NeuroImage 240 (2021) 118376

Contents lists available at ScienceDirect

NeuroImage

journal homepage: www.elsevier.com/locate/neuroimage

MoDL-QSM: Model-based deep learning for quantitative susceptibility mapping

Ruimin Feng[a], Jiayi Zhao[b], He Wang[c], Baofeng Yang[c], Jie Feng[a], Yuting Shi[a], Ming Zhang[a], Chunlei Liu[d,e], Yuyao Zhang[f], Jie Zhuang[b], Hongjiang Wei[a,g,*]

[a] School of Biomedical Engineering, Shanghai Jiao Tong University, Shanghai, China
[b] School of Psychology, Shanghai University of Sport, Shanghai, China
[c] Institute of Science and Technology for Brain-Inspired Intelligence, Fudan University, Shanghai, China
[d] Department of Electrical Engineering and Computer Sciences, University of California, Berkeley, CA, USA
[e] Helen Wills Neuroscience Institute, University of California, Berkeley, CA, USA
[f] School of Information and Science and Technology, ShanghaiTech University, Shanghai, China
[g] Institute of Medical Robotics, Shanghai Jiao Tong University, Shanghai, China

ARTICLE INFO

Keywords:
MRI – magnetic resonance imaging
QSM – quantitative susceptibility mapping
Dipole inversion
Model-based deep learning
Deep convolutional neural networks

ABSTRACT

Quantitative susceptibility mapping (QSM) has demonstrated great potential in quantifying tissue susceptibility in various brain diseases. However, the intrinsic ill-posed inverse problem relating the tissue phase to the underlying susceptibility distribution affects the accuracy for quantifying tissue susceptibility. Recently, deep learning has shown promising results to improve accuracy by reducing the streaking artifacts. However, there exists a mismatch between the observed phase and the theoretical forward phase estimated by the susceptibility label. In this study, we proposed a model-based deep learning architecture that followed the STI (susceptibility tensor imaging) physical model, referred to as MoDL-QSM. Specifically, MoDL-QSM accounts for the relationship between STI-derived phase contrast induced by the susceptibility tensor terms (χ_{13}, χ_{23} and χ_{33}) and the acquired single-orientation phase. The convolutional neural networks are embedded into the physical model to learn a regularization term containing prior information. χ_{33} and phase induced by χ_{13} and χ_{23} terms were used as the labels for network training. Quantitative evaluation metrics were compared with recently developed deep learning QSM methods. The results showed that MoDL-QSM achieved superior performance, demonstrating its potential for future applications.

1. Introduction

Quantitative susceptibility mapping (QSM) is a recent technique based on MRI phase signal that quantifies the spatial distribution of magnetic susceptibility within a tissue (Acosta-Cabronero et al., 2016; Bilgic et al., 2012; Haacke et al., 2015; Li et al., 2016; Liu et al., 2015; Schweser et al., 2013; Shmueli et al., 2009; Wang and Liu, 2015; Wharton and Bowtell, 2010). QSM computes magnetic susceptibility from phase images of gradient-recalled echoes (GRE), typically assuming that phase shift results primarily from susceptibility-induced field inhomogeneity. The susceptibility contributors include biometals and molecules, e.g., iron, calcium, lipids, and myelin. Tissue susceptibility is also a crucial biomarker of pathological processes. For example, QSM has been applied for studying a variety of neurodegenerative diseases, e.g., brain aging, baby brain development, Parkinson's disease, Alzheimer's disease, and intracranial hemorrhage (Acosta-Cabronero et al., 2013; Barbosa et al., 2015; Betts et al., 2016; Chen et al., 2014; Du et al., 2018; Lotfipour et al., 2012; Zhang et al., 2019; Zhang et al., 2018). Furthermore, QSM has the potential to achieve accurate target localization in deep brain stimulation (DBS), benefitting from the improved visualization of subthalamic nucleus (STN) and globus pallidus pars internus (GPi) (Rasouli et al., 2018; Wei et al., 2019b).

Although QSM has been demonstrated to have great potential for research purposes and clinical applications, QSM reconstruction is non-trivial. Computing susceptibility requires several processing steps involving phase unwrapping, background phase removal, and solving an inverse problem relating the tissue phase to the underlying susceptibility distribution. Among them, the dipole inversion for estimating the susceptibility map from a local tissue field map is more complicated. The field map must be deconvolved with a unit dipole kernel corre-

* Corresponding author at: School of Biomedical Engineering, Shanghai Jiao Tong University, 1954 Huashan Rd, MED-X Research Institute, Shanghai, 200030, China.
E-mail addresses: hongjiang.wei@sjtu.edu.cn, weihjhit@gmail.com (H. Wei).

https://doi.org/10.1016/j.neuroimage.2021.118376.
Received 20 January 2021; Received in revised form 2 July 2021; Accepted 7 July 2021
Available online 8 July 2021.

sponding to a pointwise division in k-space. This deconvolution is ill-posed because of zeros in the k-space dipole kernel on two conical surfaces at approximately 54.7°° relative to the B_0 direction. The inverse kernel is undefined at these surfaces and noise is amplified in regions where the kernel is very small, making a simple inversion of the forward calculation impractical. Different methods have been proposed to solve the ill-posed nature of this inverse problem. In general, QSM is solved by imposing conditions on the ill-posed inverse calculation to measure the susceptibility distribution while minimizing noise and artifacts (De Rochefort et al., 2008; Kressler et al., 2009; Liu et al., 2012; Wu et al., 2012). However, these regularization methods are considerably slow and care must be taken on the assumptions made when selecting spatial priors to avoid over-regularization and reduction of image contrast (Wharton and Bowtell, 2010).

Alternatively, another class of QSM algorithm uses multiple orientation sampling to compensate for the missing data in a single orientation, such as Calculation of Susceptibility through Multiple Orientation Sampling (COSMOS) (Liu et al., 2009) and Susceptibility Tensor Imaging (STI) (Liu, 2010). These two methods require multiple scans for one subject with rotations of head at different orientations relative to the main magnetic field. COSMOS requires at least three different scanning orientations and STI requires at least six to perform the dipole deconvolution analytically. Although both COSMOS and STI diagonal tensor element χ_{33} can be considered as the gold standard for different application purposes, the scanning time is significantly prolonged. On the one hand, this hinders their feasibility in clinical practice and increases the risk of motion artifacts, especially for the elderly and young children. On the other hand, large-angle rotations for human head in a standard tunnel magnet with multi-channel head coils are limited. Thus, the multiple orientation QSM reconstruction methods are usually impractical for clinical studies.

Recently, convolutional neural networks (CNN) have been proposed to approximate the dipole inversion process and generate high-quality QSM from single orientation phase measurements. Some of these schemes adopted the U-Net structure (Ronneberger et al., 2015) as the backbone. For example, DeepQSM trained the network by synthetic geometric images to learn the relationship between phase and susceptibility (Bollmann et al., 2019). QSMnet used realistically acquired data to learn the COSMOS-like QSM maps (Yoon et al., 2018). QSMnet+ further improved the performance of QSMnet by data augmentation that enlarged the dynamic range of the training data to overcome the underestimation of high susceptibility values in brain nuclei (Jung et al., 2020). AutoQSM aimed to predict QSM directly from total phase maps without brain masking and background phase removal (Wei et al., 2019a). Inspired by the success of Generative Adversarial Networks (GANs) (Goodfellow et al., 2014) in computer vision, QSMGAN adopted GANs to further improve reconstruction quality and accuracy (Chen et al., 2020b). Other studies of QSM reconstruction included xQSM, which trained an octave CNN to improve network generalization capability (Gao et al., 2020). All of the above deep learning methods learn the necessary features of QSM maps via a data-driven manner. More recently, researchers proposed to incorporate the physical models into CNNs to solve the dipole inversion problem. For example, Variational regularizer for Nonlinear Dipole Inversion (VaNDI) trained a variational network (Hammernik et al., 2017) to optimize the parameters in an unrolled gradient descent algorithm for non-linear dipole inversion (Polak et al., 2019). Learned Proximal CNN (LPCNN) (Lai et al., 2020) and proximal variational networks (Kames et al., 2019) combined the strengths of CNN and model-based iterative solvers to learn an implicit regularizer via proximity operator.

In this study, we proposed an STI-based deep learning architecture for single-orientation QSM reconstruction, referred to as MoDL-QSM. The main novelties of the proposed approach over related deep-learning schemes are (1) the proposed scheme accounts for the relationship between STI-derived phase induced by the rightmost column of the susceptibility tensor (χ_{13}, χ_{23} and χ_{33}) and the acquired single-orientation phase. (2) STI component, χ_{33}, was used as the training label to make the network preserve the nature of anisotropic magnetic susceptibility in brain white matter. (3) We combined the STI physical model with CNNs to learn a regularizer implicitly. (4) MoDL-QSM can simultaneously learn χ_{33} and the field induced by χ_{13} and χ_{23} terms. Our results demonstrate that χ_{33} as network label makes the model-based framework more consistent with the physical assumption of single-orientation QSM algorithms. Only when χ_{13}- and χ_{23}-induced phase contribution is added to the physical model, the single orientation acquired phase can be appropriately interpreted by the learned susceptibility distribution. Additionally, MoDL-QSM can provide superior image quality and high accuracy susceptibility quantification for healthy and diseased brain tissues.

2. Theory

2.1. Relationship between field perturbation and magnetic susceptibility

When biological tissue with susceptibility distribution χ is placed in the main magnetic field B_0, it will be magnetized and generate a magnetic field perturbation δB. Based on STI theory (Liu, 2010), χ is orientation-dependent, which can be represented by a second-order symmetric tensor, i.e., $\chi = \begin{bmatrix} \chi_{11} & \chi_{12} & \chi_{13} \\ \chi_{12} & \chi_{22} & \chi_{23} \\ \chi_{13} & \chi_{23} & \chi_{33} \end{bmatrix}$. In the subject frame of reference, the field perturbation δB is given by:

$$\mathcal{F}\delta B^{sub} = \frac{\mathcal{F}\varphi}{2\pi\gamma T_E B_0} = \frac{1}{3}(\hat{\mathrm{H}}^{sub})^{\mathrm{T}}\mathcal{F}\chi^{sub}\hat{\mathrm{H}}^{sub} - \left(\mathrm{k}^{sub}\right)^{\mathrm{T}}\hat{\mathrm{H}}^{sub}\frac{(\mathrm{k}^{sub})^{\mathrm{T}}\mathcal{F}\chi^{sub}\hat{\mathrm{H}}^{sub}}{\|\mathrm{k}^{sub}\|_2^2} \tag{1}$$

Where all superscripts in the formula indicate the coordinate system used. Standard notations indicate vector and scalar. Bold notations indicate matrix. $\mathcal{F}$ denotes the Fourier transform. γ is the gyromagnetic ratio, φ denotes tissue phase after background phase removal and T_E is the echo time. $\hat{\mathrm{H}}^{sub} = [H_1^{sub}, H_2^{sub}, H_3^{sub}]^{\mathrm{T}}$ is the unit direction vector of the applied main magnetic field. $\mathrm{k}^{sub} = [k_x^{sub}, k_y^{sub}, k_z^{sub}]^{\mathrm{T}}$ represents a spatial vector in the Fourier domain. $(\cdot)^{\mathrm{T}}$ denotes transposition and $\|\cdot\|_2$ denotes the L2 norm. When the subject frame of reference is used, χ^{sub} remains the same for each orientation and the tensor can be solved by least-squares estimation after registering each orientation to the supine one (the normal position). When the laboratory frame of reference is used, the susceptibility tensor is rotated according to the rotation matrix for different head orientations, while the magnetic field vector remains along the z-axis, i.e., $\hat{\mathrm{H}}^{lab} = [0,\ 0,\ 1]^{\mathrm{T}}$:

$$\chi^{lab} = \mathbf{R}^{\mathrm{T}}\chi^{sub}\mathbf{R} \tag{2}$$

Where $\mathbf{R}$ denotes the rotation matrix from the laboratory frame to the subject frame, which can be obtained by the registration process. For the single orientation GRE data acquisition, the imaging frame coincides with the laboratory frame. Considering the field is a function of $\mathcal{F}\chi^{lab}\hat{\mathrm{H}}^{lab}$, only the rightmost column of the tensor, $[\chi_{13}^{lab}, \chi_{23}^{lab}, \chi_{33}^{lab}]^{\mathrm{T}}$, has contributions to field perturbation. Thus, the relationship between field perturbation and susceptibility tensor in the laboratory frame of reference is simplified as:

$$\mathcal{F}\delta B^{lab} = \left[\frac{1}{3} - \frac{\left(k_z^{lab}\right)^2}{\|\mathrm{k}^{lab}\|_2^2}\right]\mathcal{F}\chi_{33}^{lab} - \frac{k_z^{lab}}{\|\mathrm{k}^{lab}\|_2^2}\left(k_x^{lab}\mathcal{F}\chi_{13}^{lab} + k_y^{lab}\mathcal{F}\chi_{23}^{lab}\right) \tag{3}$$

Where χ_{13}^{lab}, χ_{23}^{lab}, χ_{33}^{lab} are three components of the rightmost column of χ^{lab}. The field perturbation, $(\delta B')^{lab}$, derived from the off-diagonal tensor terms, χ_{13}^{lab} and χ_{23}^{lab}, can be expressed as:

$$\mathcal{F}\left(\delta B'\right)^{lab} = -\frac{k_z^{lab}}{\|\mathrm{k}^{lab}\|_2^2}\left(k_x^{lab}\mathcal{F}\chi_{13}^{lab} + k_y^{lab}\mathcal{F}\chi_{23}^{lab}\right) \tag{4}$$

Conventional single-orientation QSM algorithms assume that the phase term, $(\delta B')^{lab}$, could be negligible and mainly focus on the susceptibility component along the B_0 direction, i.e., χ_{33}^{lab} as the ground

truth susceptibility. Therefore, they aim to solve the following dipole inversion problem:

$$\mathcal{F}\delta B^{lab} = \left[\frac{1}{3} - \frac{\left(k_z^{lab}\right)^2}{\|\mathrm{k}^{lab}\|_2^2}\right]\mathcal{F}\chi_{33}^{lab} \tag{5}$$

Eq. (5) motivates the use of χ_{33}^{lab} as the label to preserve the inherent susceptibility anisotropy of brain white matter. Additionally, the contributions from χ_{13}^{lab} and χ_{23}^{lab} components to the acquired single-orientation phase signal are nonnegligible since they could rise to 70% amplitude relative to χ_{33}^{lab} component (Langkammer et al., 2018). Therefore, we take χ_{33}^{lab} and $\delta B'$ as the learning targets of MoDL-QSM to ensure that the overall framework is consistent with the STI model.

2.2. Combination of STI physical model and CNN

Taking both χ_{33}^{lab} and $\delta B'$ into account, Eq. (3) can be rewritten as the following linear equation system:

$$\delta B = \mathcal{F}^{-1}\begin{bmatrix} \frac{1}{3} - \frac{(k_z)^2}{\|\mathrm{k}\|_2^2} & 1 \end{bmatrix}\mathcal{F}\begin{bmatrix}\chi_{33}\\ \delta B'\end{bmatrix} \tag{6}$$

Note that, for simplicity, we dropped the superscript "*lab*". $\mathcal{F}^{-1}$ is the inverse Fourier transform. Let $\boldsymbol{A}$ denote the forward operator matrix and vector X denotes the voxel values of χ_{33} and $\delta B'$ to be solved.

$$\boldsymbol{A} = \mathcal{F}^{-1}\begin{bmatrix} \frac{1}{3} - \frac{(k_z)^2}{\|\mathrm{k}\|_2^2} & 1 \end{bmatrix}\mathcal{F} \tag{7}$$

$$X = \begin{bmatrix}\chi_{33}\\ \delta B'\end{bmatrix} \tag{8}$$

Then Eq. (6) can be expressed as:

$$\delta B = \boldsymbol{A}X \tag{9}$$

Solving X from δB is an ill-posed problem. One solution is to convert Eq. (9) into a minimum optimization problem:

$$\hat{X} = \underset{X}{\operatorname{argmin}}\, g(X) + R(X) \tag{10}$$

Where $g(X) = \frac{1}{2}\|\boldsymbol{A}X - \delta B\|_2^2$ is the data consistency term. $R(X)$ is the regularization term added according to prior information. Generally, $R(X)$ is L1 norm containing non-differential points. One can use the proximal gradient descent algorithm (Parikh and Boyd, 2014) to iteratively solve Eq. (10). The X in the k^{th} iteration can be expressed as:

$$\hat{X}^k = Prox_{t_k,R}\left(\hat{X}^{k-1} - t_k\nabla g\left(\hat{X}^{k-1}\right)\right) \tag{11}$$

and

$$\nabla g\left(\hat{X}^{k-1}\right) = \boldsymbol{A}^{\mathrm{H}}\left(\boldsymbol{A}\hat{X}^{k-1} - \delta B\right) \tag{12}$$

we have

$$\hat{X}^k = Prox_{t_k,R}\left(t_k\boldsymbol{A}^{\mathrm{H}}\delta B + \left(\boldsymbol{I} - t_k\boldsymbol{A}^{\mathrm{H}}\boldsymbol{A}\right)\hat{X}^{k-1}\right) \tag{13}$$

Where $Prox_{t_k,R}(\cdot)$ is the proximity operator:

$$Prox_{t_k,R}(z) = \underset{X}{\operatorname{argmin}}\left(R(z) + \frac{1}{2t_k}\|X - z\|_2^2\right) \tag{14}$$

In the above formulas, t_k is the step size in the k^{th} iteration in gradient descent. $\boldsymbol{A}^{\mathrm{H}}$ is the conjugate transpose of $\boldsymbol{A}$. $\boldsymbol{I}$ represents the identity matrix. In Eq. (14), the operator $Prox_{t_k,R}(\cdot)$ does not depend on $g(X)$, only depends on $R(X)$, indicating that the data consistency term $g(X)$ and regularization term $R(X)$ can be decoupled during the solving process. Benefitting from this advantage of proximal gradient descent algorithm, we can incorporate CNNs into Eq. (13) to train a regularization term by learning its associated proximity operator, $Prox_{t_k,R}$. The scheme of the proposed architecture is shown in Fig. 1(a). We unrolled Eq. (13) into three iterations and initialized $\hat{X}^0$=0, so the input of the network was $t_0\boldsymbol{A}^{\mathrm{H}}\delta B$. t_k in the k^{th} iteration was a learnable parameter. Three CNNs shared their weights (blue blocks in Fig. 1(a), "**C**" represents "CNN") and replaced $Prox_{t_k,R}$ with the learnable parameters. The output of each CNN performed the physical model operation (green blocks in Fig. 1(a), "**P**" represents "Physical"). The final output of MoDL-QSM consisted of two channels, χ_{33} and $\delta B'$. The regularization term was learned by minimizing the L1 loss of the two channels separately between output and label.

3. Methods

3.1. Network architecture

The network architecture is depicted in Fig. 1(b). A CNN has a total of 18 convolutional layers containing eight repetitive applications of residual learning block (He et al., 2016). For the first 17 convolutional layers, the kernel size is $3 \times 3 \times 3$ with stride 1. The batch normalization layer (BN) is used to speed up convergence. Rectified linear unit (ReLU) is adopted as the activation function. The last convolution is $1 \times 1 \times 1$ with 2 output channels to simultaneously generate χ_{33} and $\delta B'$ maps. The number of channels after each layer is summarized at the bottom of blocks and the output size is summarized at the top of blocks in Fig. 1(b).

3.2. MRI data acquisition and processing

Our training data included 5 healthy volunteers with 15~23 head orientations per subject (see Table s1 in the supplementary material for detailed head rotation degrees). The subjects were scanned at Shanghai University of Sport using a 3T scanner (Prisma, Siemens Healthcare, Erlangen, Germany) equipped with a 64-channel head coil. This experiment was approved by Shanghai Jiao Tong University Human Ethics Committee and all subjects signed informed consent before scanning. A multi-echo 3D GRE sequence was used with the following scan parameters: FOV=210 × 224 × 160 mm^3, voxel size=1 mm^3 isotropic, TR=38 ms, TE_1/spacing/TE_6=7.7/5/32.7 ms, bandwidth=190 Hz/pixel, flip angle=15°, GRAPPA factor=2, and total imaging time=8.8 minutes. For each volunteer, the scan was repeated at different head orientations.

The brain mask was generated using BET in FSL (Smith, 2002) on the magnitude images. Phase images were processed in STISuite (https://people.eecs.berkeley.edu/~chunlei.liu/software.html). First, the raw phase data was unwrapped by Laplacian-based phase unwrapping (Schofield and Zhu, 2003). Then the background phase was removed using VSHARP (Wu et al., 2012) to obtain the tissue phase. Additionally, the tissue phase from different echoes was normalized by $2\pi\gamma T_E B_0$ and averaged together to obtain the field map. Finally, the multiple orientation field maps were processed to compute the susceptibility tensor. Specifically, the magnitude images at the first T_E of different head orientations were coregistered to that of the supine position by affine transformation with 7 degrees of freedom using FSL FLIRT (Jenkinson and Smith, 2001). The transformation matrix was then applied to the corresponding field perturbation map. The orientation of the applied magnetic field $\hat{\mathrm{H}}^{sub}$ in the subject frame of reference (Eq. (1)) was calculated based on the transformation matrix. The six independent variables of the symmetric susceptibility tensor were computed voxel by voxel following the STI model (Liu, 2010). The obtained susceptibility tensor was converted to the laboratory frame of reference for each orientation according to Eq. (2). The field perturbation, $\delta B'$, induced by χ_{13} and χ_{23}, was calculated based on Eq. (4). In total, 90 pairs of input field perturbation maps and the corresponding labels were obtained.

3.3. Network Implementation

The proposed network structure was implemented using Python 3.6.2 and Keras v2.2.5 with Tensorflow as the backend and trained using one NVIDIA 1080TI GPU. To fit into GPU memory, the patch size for MoDL-QSM training was cropped to 48 × 48 × 48. The training patches were generated by randomly extracting from all 90 scans. To

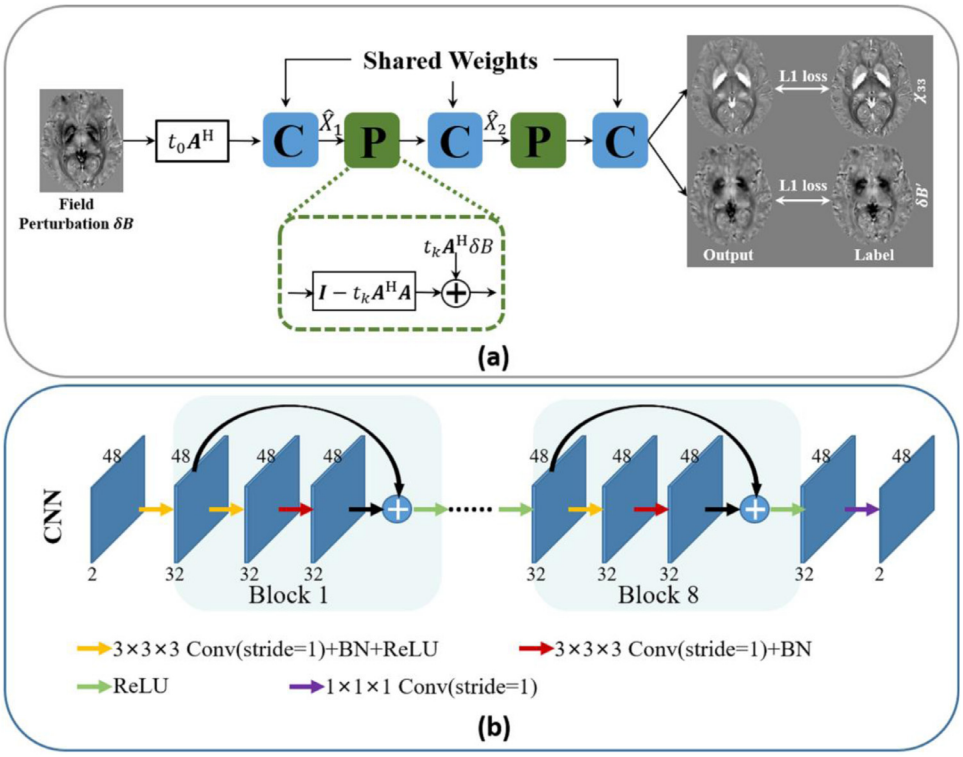

Fig. 1. Overview of the proposed MoDL-QSM architecture. (a) The schematic diagram of MoDL-QSM. Three CNNs shared their weights (blue blocks, "**C**" represents "CNN") and replaced $Prox_{t_k,R}$ with the learnable parameters. The output of each CNN performed the physical model operation (green blocks, "**P**" represents "Physical"). The final output of MoDL-QSM consisted of two channels, χ_{33} and $\delta B'$. (b) The network structure of the CNN. The number of channels after each layer is summarized at the bottom of blocks and the output size is summarized at the top of blocks.

improve training efficiency, patches with more than 20% background region were discarded. Twenty-seven thousand patches were obtained in total. 80% of them were used for training and 20% for validation. MoDL-QSM was trained for 40 epochs. The initial learning rate was 10^{-3} and reduced to half when the validation loss didn't decay in three epochs. The Adam optimizer (Kingma and Ba, 2015) was used with a batch of size 2. The total training time was about 30 hours. During the training process, 48 × 48 × 48 patches and the corresponding full-size dipole kernel ($\frac{1}{3} - \frac{(k_z)^2}{\|k\|_2^2}$) were fed into the network. To preserve high-frequency information, the 48 × 48 × 48 patches were padded to original size to match the size of dipole kernel when performing physical model operator (green blocks in Fig. 1(a)) and then were cropped back to 48 × 48 × 48.

For testing, MoDL-QSM can operate on full-size input data to save reconstruction time. If the GPU memory is not enough for the large size, a "patch-then-stitch" manner will be adopted. Specifically, the full-size images were cropped into 48 × 48 × 48 with 1/3 overlap. Then the output patches were stitched to produce complete output maps. The source codes and trained model ready for testing have been published at https://github.com/Ruimin-Feng/MoDL-QSM

3.4. Evaluation of MoDL-QSM

To demonstrate the proposed deep learning architecture with two labels is more rational than COSMOS as the training label, we conducted Experiment 1 to demonstrate the proposed method can well preserve susceptibility anisotropy of brain white matter.

Experiment 1: The original LPCNN architecture (Lai et al., 2020) was trained using the same 90 training data but with COSMOS as the label. Then the COSMOS-labeled LPCNN and χ_{33}-labeled MoDL-QSM were tested on another two subjects scanned at different orientations using the same scan parameters as the training data.

Then, to evaluate the reconstruction performance of MoDL-QSM, different datasets were used. Since these datasets differ from the training data in terms of acquisition parameters, vendors, signal-to-noise ratio (SNR), etc., the following experiments could test MoDL-QSM's robustness to these interference factors and further illustrate MoDL-QSM's ability to learn the regularization term in the physical model. Besides, the predicted χ_{33} maps were also compared with conventional and deep learning-based methods, e.g., Thresholded K-space Division (TKD) (Shmueli et al., 2009), STAR-QSM (Wei et al., 2015), AutoQSM (Wei et al., 2019a), and QSMnet (Yoon et al., 2018). The threshold in TKD method was 0.2 as suggested in the original paper. AutoQSM and QSMnet presented here were both retrained using χ_{33} as the label calculated from our training data.

Experiment 2: 35 scans from another two healthy volunteers (18 head orientations for the first volunteer and 17 head orientations for the second volunteer. See Table s2 for the detailed head rotation degrees) were acquired using the same scanner and imaging parameters as the training data. Three quantitative metrics: root mean squared error (RMSE), structure similarity index (SSIM) (Zhou et al., 2004), and high-frequency error norm (HFEN) (Ravishankar and Bresler, 2011) were computed on these 35 scans and compared between different methods. To further demonstrate the quantitative accuracy of MoDL-QSM in deep gray matters (DGMs). Five regions of interest (ROIs), putamen (PUT), globus pallidus (GP), caudate nucleus(CN), red nucleus (RN), and substantia nigra (SN) were segmented by registering a QSM atlas (Zhang et al., 2018) to the 35 individual subjects. For each ROI, the mean and standard deviation of susceptibility reconstructed by different methods were displayed. To illustrate MoDL-QSM's ability to facilitate the physical model of single-orientation QSM reconstruction, we compared the differences between the forward-simulated phase generated by susceptibility maps of different methods with the acquired phase. The output of AutoQSM (only χ_{33}), QSMnet (only χ_{33}), LPCNN (COSMOS) and MoDL-QSM ($\chi_{33} + \delta B'$) were used to calculate the simulated phase maps based on their corresponding forward models, respectively. Then difference maps between the simulated phase maps and the acquired single-orientation phase maps were calculated. Mean and standard deviation of L1 errors between the simulated phase maps and the acquired single-orientation phase maps from the 35 scans were reported.

Experiment 3: 2016 QSM challenge data was also used to test the reconstruction performance of AutoQSM, QSMnet, and MoDL-QSM. The reference image χ_{33} was used as ground truth as proposed in the original paper (Langkammer et al., 2018). For quantitative comparison, RMSE, SSIM, and HFEN for the three methods were calculated.

Experiment 4: To explore the potential clinical applications of MoDL-QSM, pathological data including hemorrhage, multiple sclerosis (MS), and micro-bleeding were used for testing. The data acquisition experiments were approved by Shanghai Jiao Tong University Human Ethics Committee and all subjects signed informed consent before scanning. The hemorrhage data were acquired using a 3D GRE sequence on a 3T GE HDxt MR scanner at Shanghai Ruijin Hospital with the following parameters: matrix size=256 × 256 × 66, voxel size=0.86 × 0.86 × 2 mm^3, TR=42.58 ms, TE_1/spacing/TE_{16}=3.2/2.4/39.5 ms, bandwidth=488.28 Hz/pixel, flip angle=12°. The patients with MS were acquired using a 3D GRE sequence on a 3T GE HDxt MR scanner at Shanghai Renjin Hospital with the following parameters: matrix size=256 × 256 × 124, voxel size=1 mm^3 isotropic, TR=32.36 ms, TE_1/spacing/TE_{12}=3.2/2.4/29.2 ms, bandwidth=488.28 Hz/pixel, flip angle=12°. The micro-bleeding data were acquired using a 3D GRE sequence on a 3T Philips MR scanner at Shanghai Ruijin Hospital with the following parameters: matrix size=256 × 256 × 136, voxel size=0.86 × 0.86 × 1 mm^3, TR=45 ms, TE_1/spacing/TE_{16}=3.3/2.5/41.9 ms, bandwidth=541 Hz/pixel, flip angle=12°.

Experiment 5: To test MoDL-QSM's ability for susceptibility reproducibility across different sites. Ten traveling healthy volunteers were scanned at four different sites (Shanghai Huashan Hospital, Institute of Brain and Intelligence Technology, Shanghai Jiao Tong University, and The Second Affiliated Hospital of Zhejiang University) on four 3T scanners (UIH uMR790, Shanghai, China) using a 3D GRE sequence with the following parameters: matrix size=318 × 336 × 74, voxel size=0.65 × 0.65 × 2 mm^3, TR=34.6 ms, TE_1/spacing/TE_8=3.3/3.7/29.2 ms, bandwidth=280 Hz/pixel, flip angle=15°. The data acquisition experiments were approved by Shanghai Jiao Tong University Human Ethics Committee and all subjects signed informed consent before scanning. The susceptibility maps were reconstructed by STAR-QSM and MoDL-QSM, respectively. Quantitatively, three DGMs: PUT, GP, and CN were segmented by registering a QSM atlas (Zhang et al., 2018) to each individual. The intraclass correlation coefficient (ICC) for repeated measurements was calculated using the SPSS (IBM Corp. Released 2012. IBM SPSS Statistics for Windows, Version 21.0. Armonk, NY: IBM Corp). A higher ICC indicates that the QSM reconstruction method can produce more similar susceptibility across the four sites. ICC in the range of 0 to 0.2 is considered to be slight, 0.2 to 0.4 is fair, 0.4 to 0.6 is moderate, 0.6 to 0.8 is substantial, 0.8-1.0 is almost perfect (Landis and Koch, 1977; Zuo and Xing, 2014).

Experiment 6: This experiment aims to test MoDL-QSM's performance on the data acquired at different field strengths. Ten healthy volunteers were scanned using a 3D Fast Low Angle SHot (FLASH) sequence on a whole-body 7T scanner at Fudan University (Terra; Siemens Healthineers, Erlangen, Germany) equipped with a 32-channel head coil with the following parameters: matrix size=308 × 358 × 160, voxel size=0.6 × 0.6 × 1 mm^3, TR=28 ms, TE_1/spacing/TE_5=4/5/24 ms, bandwidth=305 Hz/pixel, flip angle=15°. The data acquisition experiments were approved by Shanghai Jiao Tong University Human Ethics Committee and all subjects signed informed consent before scanning. Susceptibility maps were reconstructed by STAR-QSM, AutoQSM, QSMnet, and MoDL-QSM, respectively. To compare the delineation of small deep gray nuclei from surroundings on the QSM images reconstructed by different methods, the regions containing STN and GPi were zoomed in and the susceptibility profiles from STN to SN were plotted.

4. Results

4.1. Comparison of susceptibility accuracy produced by COSMOS- and χ_{33}- labeled networks

Fig. 2 compares COSMOS, COSMOS-labeled LPCNN output, χ_{33}, and χ_{33}-labeled MoDL-QSM output on one healthy subject at four representative head orientations. Fig. 2(a) shows a representative axial slice with a manually selected ROI marked by the blue line. Fig. 2(b) are zoomed-in images of the region outlined by the white box as shown in Fig. 2(a). Visually, the white matter fibers indicated by yellow arrows show similar contrast between orientations on COSMOS maps. However, the QSM maps predicted by COSMOS-labeled LPCNN exhibit a clear difference between Orientation 2 and Orientation 3, indicating a clear mismatch with the labels. In contrast, MoDL-QSM can effectively preserve this underlying white matter susceptibility anisotropy, consistent with that in the labels χ_{33}, as pointed by red arrows. For quantitative comparisons, the white matter fiber was selected as an ROI (highlighted by the blue line in Fig. 2(a)) to calculate the mean susceptibility values. A *t*-test was performed for statistical analysis. The statistically significant difference was determined based on the threshold of 0.05. As shown in Fig. 2(c), COSMOS shows identical susceptibility across four orientations. In contrast, COSMOS-labeled LPCNN output, χ_{33}, and χ_{33}-labeled MoDL-QSM output exhibit susceptibility variations between orientations. Except for COSMOS, the other three results showed significant differences in susceptibility between Orientation 2 and Orientation 3 (P =0.99 for COSMOS, P <0.001 for COSMOS-labeled LPCNN output, P <0.001 for χ_{33}, and P<0.001 for χ_{33}-labeled MoDL-QSM output). Additionally, there were significant differences between COSMOS and COSMOS-labeled LPCNN output (P=0.003 for Orientation 1, P =0.003 for Orientation 2, and P <0.001 for Orientation 3). However, no statistically significant differences were found between χ_{33} and χ_{33}-labeled MoDL-QSM output for four orientations (P =0.12 for Orientation 1, P =0.08 for Orientation 2, P =0.54 for Orientation 3, P =0.84 for Orientation 4), demonstrating the susceptibility anisotropy can be well preserved in χ_{33}-labeled MoDL-QSM in brain white matter.

Table 1
Quantitative performance metrics, RMSE, SSIM, and HFEN from the five different QSM reconstruction methods referenced to the label χ_{33}. MoDL-QSM shows better performances in all criteria than other methods.

	RMSE	SSIM	HFEN
TKD	92.42±3.99	0.7753±0.0165	90.23±3.65
STAR-QSM	79.57±3.27	0.8180±0.0160	77.26±2.81
AutoQSM	69.40±2.68	0.8549±0.0193	70.04±2.73
QSMnet	55.07±3.24	0.8759±0.0141	54.39±2.70
MoDL-QSM	**54.86±3.10**	**0.8801±0.0140**	**54.31±2.87**

4.2. Evaluation of MoDL-QSM's performance

Fig. 3(a) shows three orthogonal views of QSM images on one healthy subject using five QSM reconstruction methods. Fig. 3(b) shows the zoomed-in images of the region outlined by the red box in Fig. 3(a). The small cortical gray matter structure is more clearly observed on the QSM maps of MoDL-QSM results and label, as pointed by the yellow arrows. Fig. 3(c) displays the difference maps between the QSM maps reconstructed from different methods with respect to the label χ_{33}. AutoQSM shows relatively larger differences in the cortex (the green arrow) and QSMnet shows relatively larger differences primarily in DGMs (the blue arrow). The quantitative metrics: RMSE, SSIM, HFEN of the five reconstruction methods are summarized in Table 1. The results of MoDL-QSM achieved the lowest RMSE with 54.86, the highest SSIM with 0.8801, and the lowest HFEN with 54.31, suggesting the best performances based on these criteria.

Fig. 4 compares the regional susceptibility values in selected DGMs computed by different QSM reconstruction methods. Compared with the labels, STAR-QSM and QSMnet show underestimated susceptibility values in DGMs. In contrast, AutoQSM and MoDL-QSM have better predictions for susceptibility estimations.

Fig. 5 illustrates the reconstruction results using AutoQSM, QSMnet, and MoDL-QSM on the 2016 QSM challenge data. The results of AutoQSM and QSMnet have larger errors in GP than MoDL-QSM's results (Mean square errors in GP: 0.0097 for AutoQSM, 0.0046 for QSMnet,

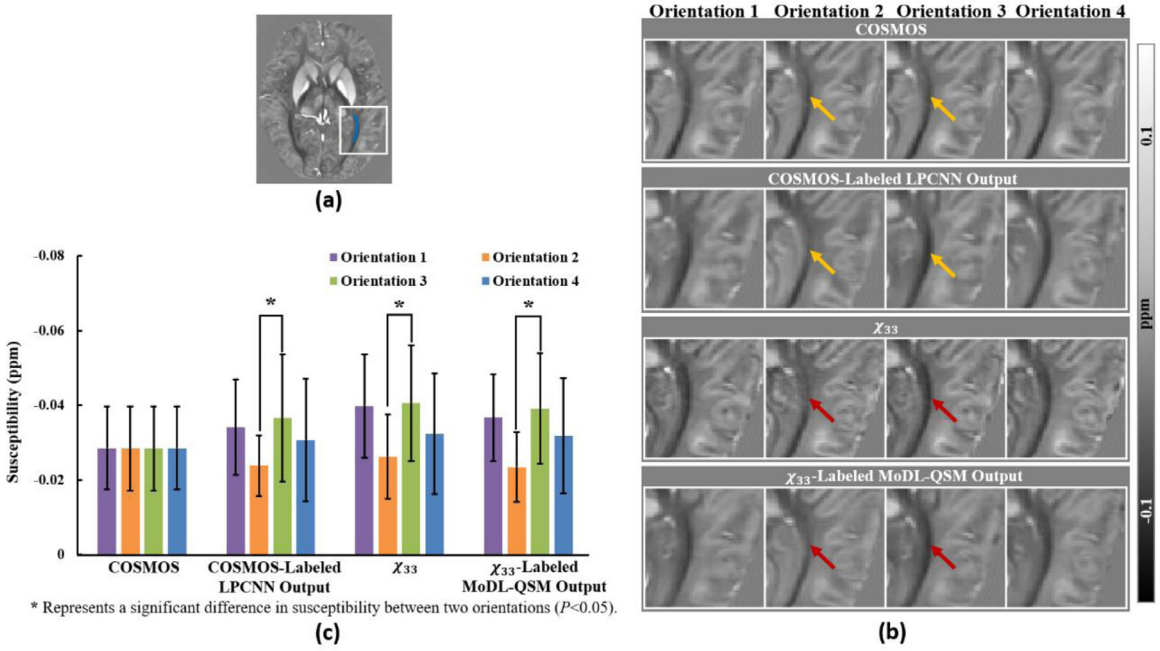

Fig. 2. Comparisons of COSMOS, COSMOS-labeled LPCNN output, χ_{33}, and χ_{33}-labeled MoDL-QSM output on the same subject at four different head orientations. (a) A representative axial slice. (b) Zoomed-in images of the region outlined by the white box in (a). Yellow arrows point to the white matter fiber bundles that show similar contrast in COSMOS while showing different contrast in COSMOS-labeled LPCNN output at Orientation 2 and Orientation 3. Red arrows point to the preserved susceptibility anisotropy of white matter fiber bundles in both χ_{33} and χ_{33}-labeled MoDL-QSM output. (c) Mean susceptibility values of the white matter fiber highlighted by the blue line in (a). COSMOS shows identical susceptibility at four orientations. In contrast, COSMOS-labeled LPCNN output, χ_{33}, and χ_{33}-labeled MoDL-QSM output exhibit consistent susceptibility changes. Except for COSMOS, the other three results show significant differences in susceptibility between Orientation 2 and Orientation 3 (P <0.05).

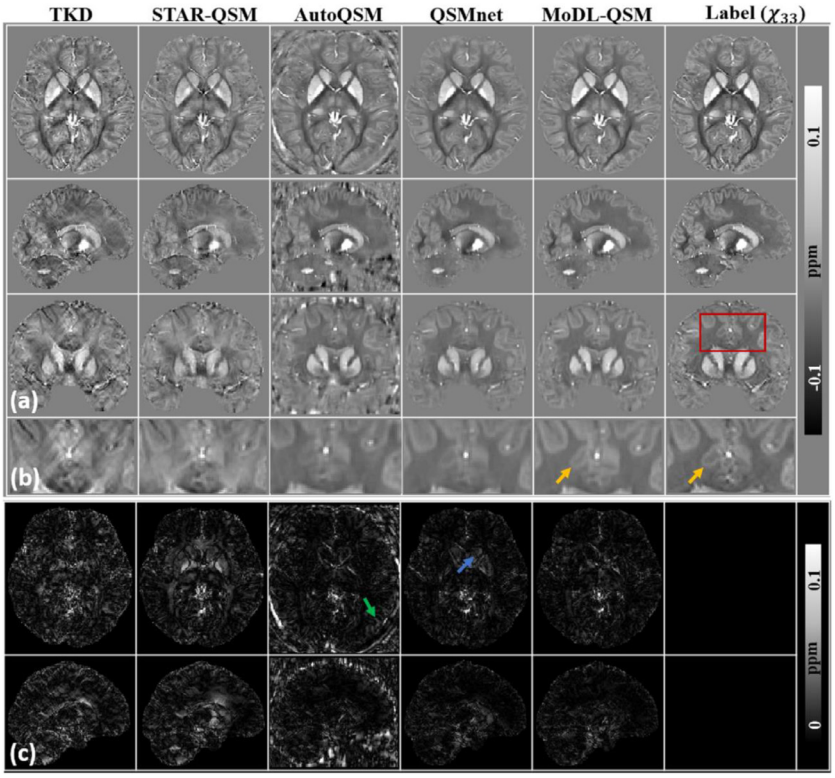

Fig. 3. Comparisons of different QSM reconstruction methods on a healthy subject. (a) The results are displayed in three orthogonal views. (b) Zoomed-in images of the region outlined by the red box in (a). (c) The difference maps between different reconstruction results and χ_{33} labels. Green arrow points to the larger differences in AutoQSM maps. Blue arrow points to the predicted errors in the DGM on QSMnet maps.

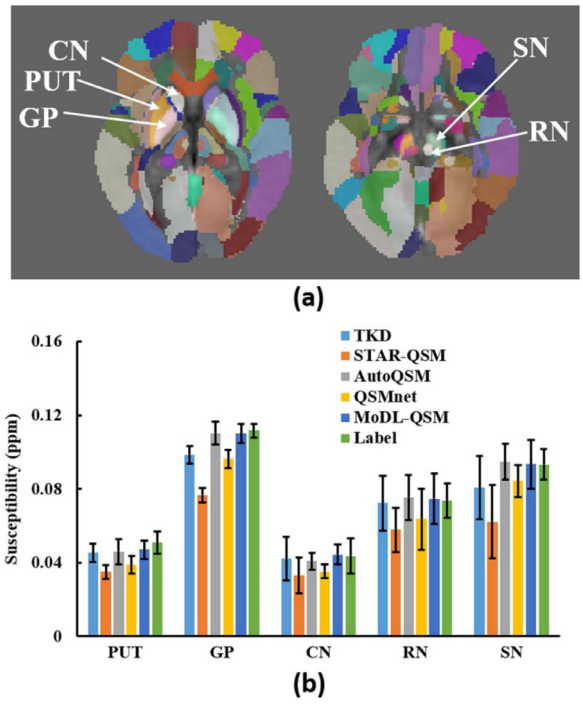

Fig. 4. ROI analysis from 35 field maps of different QSM reconstruction methods. (a) QSM atlas used for ROI segmentation. (b) The susceptibility values in the ROIs (PUT, GP, CN, RN, SN). Data are presented as mean±standard deviation. The MoDL-QSM's results match well with the label.

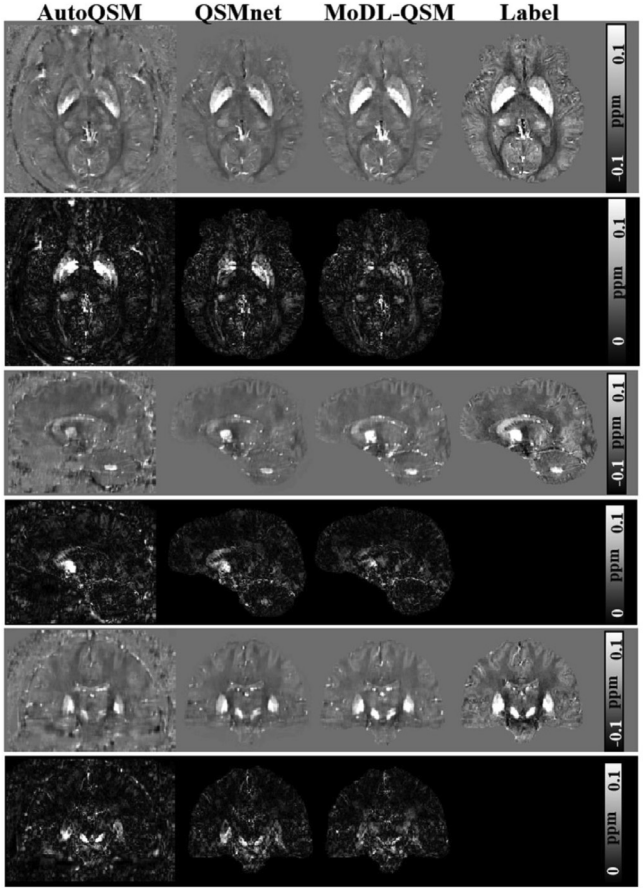

Fig. 5. Comparisons of different QSM reconstruction methods on the 2016 QSM challenge data. The error maps of MoDL-QSM show smaller differences relative to the label than the compared methods.

Table 2
Quantitative performance metrics, RMSE, SSIM, and HFEN on the 2016 QSM challenge data using AutoQSM, QSMnet, and MoDL-QSM. MoDL-QSM shows better RMSE and SSIM scores than other QSM methods and a relatively higher HFEN than QSMnet.

	RMSE	SSIM	HFEN
AutoQSM	78.99	0.8282	73.83
QSMnet	71.06	0.8386	**66.93**
MoDL-QSM	**67.91**	**0.8446**	67.04

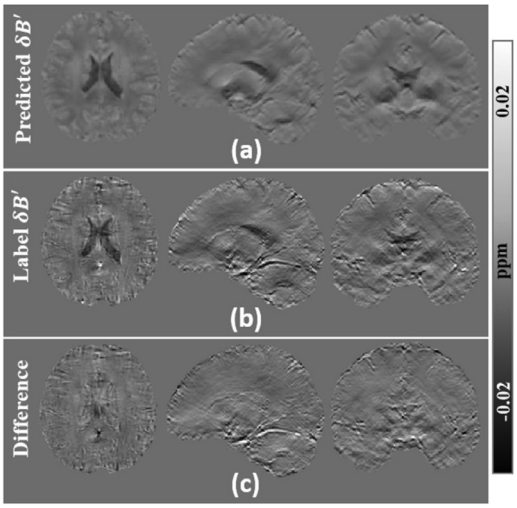

Fig. 6. Comparisons between predicted $\delta B'$ and label. (a) The predicted $\delta B'$ by MoDL-QSM. (b) The corresponding labels. (c) Difference maps.

and 0.0026 for MoDL-QSM). RMSE, SSIM, and HFEN from the three different QSM reconstruction methods are summarized in Table 2. MoDL-QSM performs lowest RMSE with 67.91, highest SSIM with 0.8446, indicating better reconstruction results than the other two methods.

4.3. *Effectiveness of* δB′ *reconstruction*

Fig. 6(a) and Fig. 6(b) display the predicted $\delta B'$ by MoDL-QSM and the corresponding labels on one healthy subject. The predicted results by MoDL-QSM reveal comparable contrast to those observed in the label. As shown in the difference maps (Fig. 6(c)), there are negligible differences related to gray and white matter. The major discrepancies that are found on the difference maps may be associated with flow effects in this non-flow compensated acquisition.

Fig. 7 compares the inconsistency between the acquired single-orientation phase and the forward-simulated phase from the predicted susceptibility. Fig. 7(a) shows the simulated phase maps calculated from results of AutoQSM, QSMnet, LPCNN, and MoDL-QSM. The difference maps between the simulated phases and the acquired single-orientation phase are shown in Fig. 7(b). The clear differences between gray and white matter as well as within the ventricle were observed on the results of AutoQSM, QSMnet, and LPCNN. In contrast, MoDL-QSM based phase error map contains no large-scale anatomical features. L1 errors ($\times 10^{-3}$) between the simulated phase maps and the acquired single-orientation phase maps from 35 test data on two subjects were reported at the bottom of Fig. 7(b), the phase maps based on MoDL-QSM results achieved the lowest error ($2.88\pm0.09 \times 10^{-3}$, $3.30\pm0.13 \times 10^{-3}$, $3.93\pm0.16 \times 10^{-3}$, and $4.05\pm0.16 \times 10^{-3}$ for MoDL-QSM, LPCNN, QSMnet, and AutoQSM, respectively.).

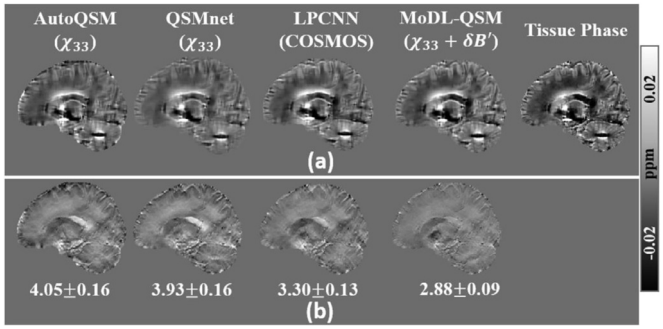

Fig. 7. (a) The forward-simulated phases calculated using outputs of different networks. (b) The difference maps of forward-simulated phase from AutoQSM, QSMnet, LPCNN, and MoDL-QSM with respect to the single-orientation acquired phase. L1 errors ($\times 10^{-3}$) of each network are reported under the images.

Table 3
The regional ICC of susceptibility values from four repeated scans. The susceptibility maps reconstructed by MoDL-QSM reveal higher ICC than STAR-QSM in both left and right sides of three selected ROIs.

	GP ICC (Right/Left)	PUT	CN
STAR-QSM	0.700/0.819	0.904/0.893	0.731/0.639
MoDL-QSM	**0.932/0.902**	**0.926/0.904**	**0.946/0.896**

4.4. The practical applications of MoDL-QSM

MoDL-QSM was also tested on patients with hemorrhage, MS, and micro-bleeding, which were not used in the training dataset. The results of STAR-QSM exhibit residual blooming artifacts around the hemorrhage lesion as indicated by the blue arrow, while AutoQSM, QSMnet, and MoDL-QSM can well suppress these shadow artifacts (Fig. 8). For MS data, all QSM reconstruction methods can detect the lesion regions, and small lesions can be better visible on the results of MoDL-QSM as indicated by blue and purple arrows (Fig. 9). When applied to the patient with micro-bleeding (Fig. 10), the lesion area is similarly delineated from surroundings by all the methods as pointed by red arrows.

Fig. 11 shows susceptibility maps from one representative traveling subject scanned on four sites reconstructed by STAR-QSM and MoDL-QSM, respectively. The susceptibility values within CN vary between different sites on STAR-QSM maps, as pointed by the red arrows. In contrast, MoDL-QSM results reveal a more consistent susceptibility contrast in CN among different sites. Quantitatively, the regional ICC of susceptibility values from four repeated scans was reported in Table 3. The susceptibility maps reconstructed by MoDL-QSM reveal higher ICC than STAR-QSM in three selected DGMs, suggesting that MoDL-QSM has better reproducibility in DGMs for the same subjects in different scanning conditions.

Fig. 12 shows the reconstruction results on the 7T dataset using STAR-QSM, AutoQSM, QSMnet, and MoDL-QSM. As shown in the zoomed-in images, the STN, SN, GPi, and GPe (i.e., globus pallidus externus) can be observed on the QSM maps of the four methods. Fig. 12(b) plots the susceptibility profiles along the green line crossing STN and SN in Fig. 12(a), the susceptibility change along the profile in STAR-QSM and MoDL-QSM images is relatively sharper than that in AutoQSM and QSMnet, indicating STN and SN can be better distinguished by these two methods. It should be noted that STAR-QSM suffers from artifacts around STN and SN.

5. Discussion

In this study, we proposed a model-based deep learning framework for QSM reconstruction. We incorporated the susceptibility tensor components into our proposed scheme for network training and the results showed several advantages over the state-of-the-art QSM methods: (1) the proposed deep-learning scheme accounts for the relationship between STI-derived phase induced by the rightmost column of the susceptibility tensor (χ_{13}, χ_{23} and χ_{33}) and the acquired single-orientation phase. (2) STI component, χ_{33}, was used as the training label to make the network preserve the nature of anisotropic magnetic susceptibility in brain white matter. (3) MoDL-QSM can simultaneously produce χ_{33} and the field perturbation induced by χ_{13} and χ_{23} terms. Our results showed that MoDL-QSM provided a more proper ground truth susceptibility for single-orientation QSM reconstruction. Testing on the healthy and diseased brain datasets demonstrates the superiority of MoDL-QSM over the compared methods.

Most of the current implementations of deep learning QSM utilize COSMOS as the ground truth susceptibility. COSMOS models susceptibility as an isotropic property, ignoring the anisotropic nature of susceptibility in white matter. Thus, COSMOS susceptibility maps would not provide an accurate reference for single-orientation QSM. To mitigate this orientation bias in white matter, we chose susceptibility tensor elements as the label for training our network. As shown in Fig. 2, the observed susceptibility contrast in COSMOS-labeled LPCNN output is not consistent with the COSMOS label at each orientation. This is mainly because that COSMOS susceptibility reflects the effective magnetic susceptibility by averaging dipole kernels of different orientations. For model-based deep learning, the network is embedded into the physical model to learn a regularization term. In the QSM reconstruction physical model, only dipole kernel from one orientation is available. Thus, the network output preserves susceptibility anisotropy at that orientation as illustrated in Fig. 2. Unlike COSMOS, STI uses a second-order symmetric tensor to characterize the susceptibility anisotropy, where χ_{33} represents the apparent susceptibility along the z-axis. In this study, χ_{33} in the laboratory frame of reference was considered as the ground truth susceptibility for single-orientation QSM reconstruction. The consistent susceptibility changes in χ_{33} and MoDL-QSM's output (Fig. 2(c)) further demonstrate that χ_{33} can mitigate the susceptibility bias in brain white matter. Therefore, we collected data from a wide range of head orientations to reconstruct high-quality STI maps and used χ_{33} as the label for network training.

Taking the tensor components of χ_{13} and χ_{23} into account, the proposed deep-learning scheme can improve the network's performance. Traditional QSM reconstruction methods ignore the contributions of χ_{13} and χ_{23} terms to the measured phase, and consider the tissue phase completely from χ_{33}. In this study, we used CNN to learn the regularization term that can simultaneously reconstruct χ_{33} and the field perturbation $\delta B'$ induced by χ_{13} and χ_{23}. Therefore, the framework of MoDL-QSM was more consistent with STI physical model. Additionally, quantitative performance metrics (Table 1) and ROI analysis (Fig. 4) demonstrated that MoDL-QSM benefits the incorporation of $\delta B'$ into the proposed architecture. The results of $\delta B'$ from MoDL-QSM show smoother contrast compared with the label (Fig. 6). One possible reason is that the quality of label $\delta B'$ map varies significantly between orientations due to the artifacts in χ_{13} and χ_{23}, while network training acts as a regression process. In practice, the contribution of $\delta B'$ to the measured phase mostly comes from microstructure effects, which may have orientation dependency. Other potential sources of errors such as vascular flux and motion might also be considered. Despite the imperfection, the forward-simulated phase from MoDL-QSM is more consistent with the acquired phase, demonstrating the phase contribution from $\delta B'$ is nonnegligible.

In MoDL-QSM, the proximal gradient descent process was unrolled into 3 iterations. Different iteration numbers were also investigated and the quantitative performance metrics of χ_{33} and $\delta B'$ were reported in Table s3 and Table s4 (see supplementary material). The reconstruction performance was improved as we increased the number of iterations from 2 to 3. However, keeping increasing the iteration number from 3 to 4 did not lead to a sustained improvement for both χ_{33} and $\delta B'$. This might be because MoDL-QSM shares weights across iterations and in-

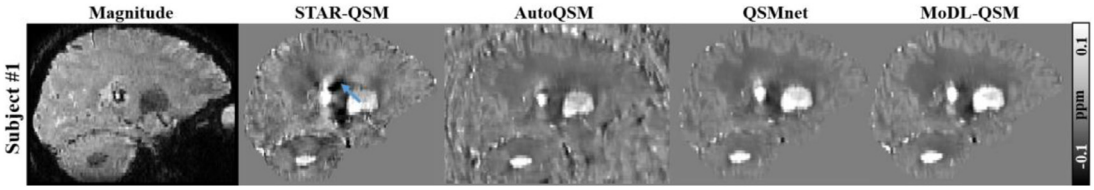

Fig. 8. Representative sagittal slices of QSM images computed using STAR-QSM, AutoQSM, QSMnet, and MoDL-QSM on a patient with hemorrhage. The QSM image of STAR-QSM exhibits blooming artifacts (indicated by the blue arrow) around the lesion, while AutoQSM, QSMnet, and MoDL-QSM can well suppress these shadow artifacts.

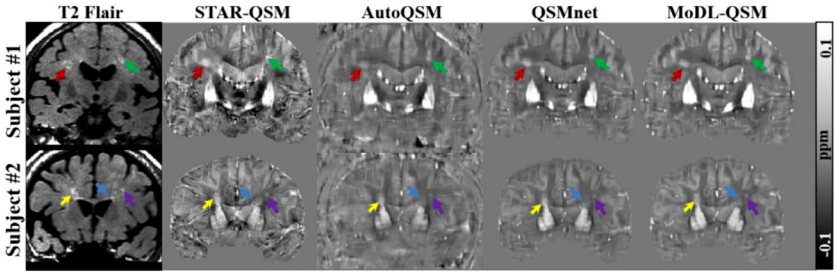

Fig. 9. Representative coronal slices of QSM images computed using STAR-QSM, AutoQSM, QSMnet, and MoDL-QSM on two MS patients. The arrows point to the MS lesions.

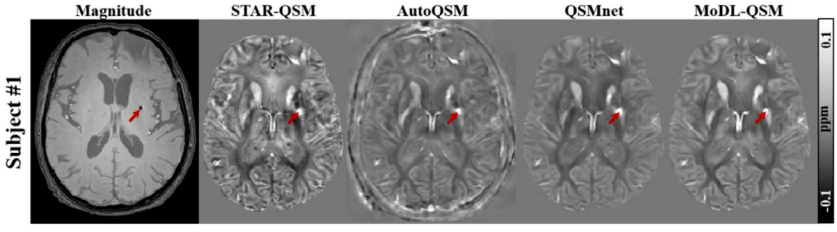

Fig. 10. Representative axial slices of QSM images computed using STAR-QSM, AutoQSM, QSMnet, and MoDL-QSM on a patient with micro-bleeding. The lesion area (red arrow) is similarly delineated in all the methods.

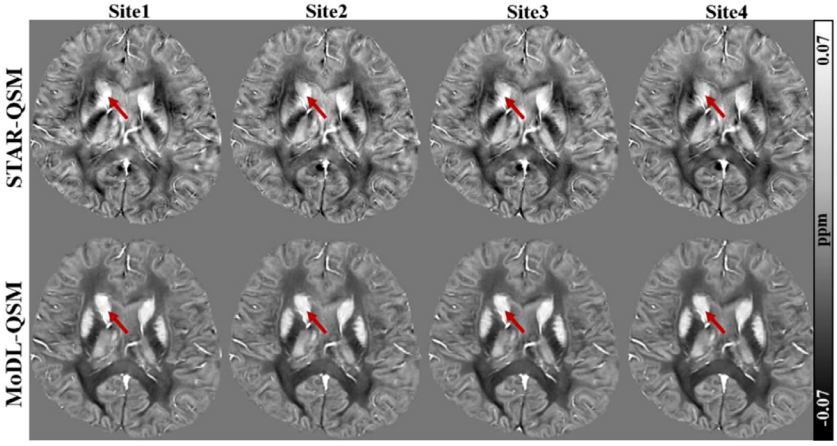

Fig. 11. Susceptibility maps from a traveling subject scanned at four sites reconstructed by STAR-QSM and MoDL-QSM. Red arrows indicate the susceptibility values within CN vary between sites on STAR-QSM maps. In contrast, MoDL-QSM results reveal a more consistent susceptibility contrast.

creasing iterative process makes it more complicated to learn a common regularization term between the inputs and outputs in each iteration. In the future, more efforts are needed to compare the reconstruction performance in the weight-shared MoDL-QSM and non-shared MoDL-QSM.

On the 2016 QSM challenge data, MoDL-QSM shows a slightly higher HFEN compared with QSMnet (Table 2). The 2016 QSM challenge data was acquired using a 3D GRE sequence with an R=15 fold accelerated Wave-CAIPI acquisition (Bilgic et al., 2016), which has a lower SNR compared to our training data. Please note that we are ignoring noise effects in the MoDL-QSM estimations as sources of errors. The regularizer learned by MoDL-QSM may degrade performance when processing the input phases with much higher noise levels. QSMnet shows a slightly lower HFEN than MoDL-QSM when testing on this challenge data. One possible reason is that the convolution kernel size used in QSMnet is 5 × 5 × 5, which has a larger receptive field than the kernel size of 3 × 3 × 3. A relatively large receptive field allows the network to capture more non-local phase information. However, it will greatly increase the model size and computational cost (Szegedy et al., 2016). MoDL-QSM achieves better performance regarding RMSE and SSIM, demonstrating the superiority of MoDL-QSM to other compared methods.

The results of hemorrhage data showed that MoDL-QSM could well delineate lesion boundaries and suppress artifacts around large susceptibility sources (Fig. 8). The MS lesion boundaries were clearly visible on MoDL-QSM images but showed ambiguity on STAR-QSM images (Fig. 9), suggesting the potential of MoDL-QSM in detecting and characterizing small MS lesions in clinical applications.

Furthermore, the multicenter traveling subject experiment was also carried out in this study. In the repeated scans at four sites, the traveling subjects were scanned in the normal supine position. Therefore, the head orientation related to the main magnetic field could be sim-

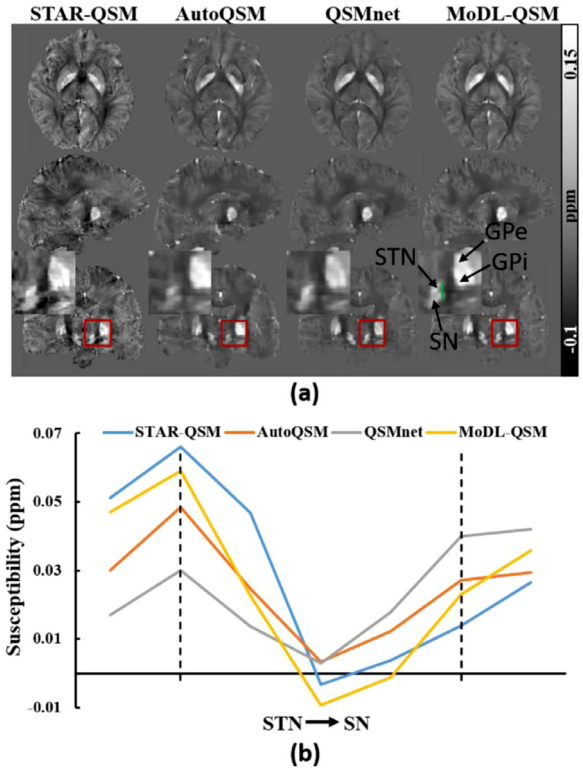

Fig. 12. One representative 7T dataset reconstructed by STAR-QSM, AutoQSM, QSMnet, and MoDL-QSM. (a) Three orthogonal views and zoomed-in images of the region outlined by the red box containing STN and GPi. (b) Susceptibility profiles along the green line crossing STN and SN in (a). The susceptibility change in STAR-QSM and MoDL-QSM is relatively sharper than that in AutoQSM and QSMnet.

ilar between scans. Additionally, DGMs with mainly iron deposits are considered to be isotropic tissues. Therefore, the susceptibility in DGMs should be identical between different scans. As shown in Fig. 11, the susceptibility of CN in STAR-QSM maps varies between scans while that in MoDL-QSM maps is more consistent. The higher ICC values across different sites in three DGMs of MoDL-QSM further support these observations quantitatively. The results indicate that MoDL-QSM is more robust to the interferences, e.g., the distance between head position and coil, thermal noise level when the subjects were scanned longitudinally. The advantages of high reproducibility and less quantification error demonstrate MoDL-QSM's potential for reliable longitudinal measurements of susceptibility time courses, enabling more precise monitoring for metal ions accumulation in neurodegenerative disorders, e.g., Parkinson's disease and Alzheimer's disease.

The content of cortical iron has been increasingly recognized as a biomarker in Alzheimer's disease and cognitive decline (Bulk et al., 2018; Chen et al., 2020a; Damulina et al., 2020; van Duijn et al., 2017). However, the artifacts between cortical gray and white matter provided by conventional reconstruction methods hinder QSM's precision in cortical iron quantification. In this study, the results of MoDL-QSM showed that artifacts in the cortical areas could be well suppressed and gray-white matter boundaries can be revealed (Fig. 2&3). This outcome may provide great potential to achieve iron quantification in the high-resolution *ex vivo* cortex and in the superficial white matter (Kirilina et al., 2020), which is helpful to further investigate the pathogenesis of Alzheimer's disease.

The benefit of ultrahigh-field 7T for QSM has been recognized as increasing interest (Bian et al., 2016; Li et al., 2012). However, the MRI signal acquired at 7T is more sensitive to field inhomogeneity and suffers from more rapid decay that causes a higher noise level when high-resolution data is required. These factors bring challenges to the dipole inversion problem for high-quality QSM. The resulting images suffer from poor quality and streaking artifacts around the region with large susceptibility variations. As illustrated in Fig. 12, the STAR-QSM results show artifacts around STN and GPi. While these artifacts on MoDL-QSM maps are invisible, suggesting MoDL-QSM can provide confident tissue structural boundaries. The improved visualization makes it possible for 7T QSM to guide DBS, which is valuable since the accurate electrode localization has been proven critical for a successful outcome, such as STN and GPi DBS for Parkinson's disease patients (Kelman et al., 2010).

The trained MoDL-QSM has some limitations. Firstly, MoDL-QSM takes both χ_{33} and $\delta B'$ into account to make the proposed framework more consistent with STI physical model. However, the tissue phase originates not only from magnetic susceptibility but also from the chemical shift (Kuchel et al., 2003), chemical exchange (Shmueli et al., 2011), and complex tissue microstructure (Wharton and Bowtell, 2012). These sources are not considered in the STI model or might be incorrectly assigned to STI components. Secondly, in Fig. 7, we demonstrated $\delta B'$ is a part of field perturbation that could not be ignored. The potential sources and applications of $\delta B'$ need to be further investigated.

6. Conclusion

We proposed an STI model-based deep learning framework for single-orientation QSM reconstruction. We first demonstrated that χ_{33} is more rational as the label than COSMOS. Thanks to the powerful feature extraction and characterization ability of CNN, we incorporate both χ_{33} and phase contributions from χ_{13} and χ_{23} to force MoDL-QSM to follow the STI model. Qualitative and quantitative comparisons show that MoDL-QSM has superior reconstruction performance than compared QSM methods. MoDL-QSM offers a way to generate high-quality QSM and may provide clinical values for well characterizing the lesions, e.g., MS or providing high fidelity anatomical delineation of brain nucleus for DBS targeting.

Credit authorship contribution statement

Ruimin Feng: Conceptualization, Methodology, Writing – original draft, Writing – review & editing. **Jiayi Zhao:** Investigation, Writing – original draft. **He Wang:** Investigation, Writing – original draft. **Baofeng Yang:** Investigation, Writing – original draft. **Jie Feng:** Validation, Writing – original draft. **Yuting Shi:** Validation, Writing – original draft. **Ming Zhang:** Validation, Writing – original draft. **Chunlei Liu:** Resources, Writing – original draft. **Yuyao Zhang:** Resources, Writing – original draft. **Jie Zhuang:** Investigation, Writing – original draft. **Hongjiang Wei:** Conceptualization, Methodology, Writing – original draft, Writing – review & editing, Supervision, Project administration, Funding acquisition.

Acknowledgments

This study is supported by the National Natural Science Foundation of China (61901256, 91949120, 62071299) and the Science and Technology Commission of Shanghai Municipality under Grant 20DZ2220400.

Data and Code Availability Statement

MoDL-QSM: Model-based Deep Learning for Quantitative Susceptibility Mapping

Data: All imaging experiments were approved by Shanghai Jiao Tong University Human Ethics Committee. Parts of the test data have been published at GitHub. The remaining test data and training data can be made available upon reasonable request to the corresponding author.

Code: The source codes and trained networks ready for testing on the phase data have been published at: https://github.com/Ruimin-Feng/MoDL-QSM

This repository contains all necessary instructions, codes, and data to test MoDL-QSM.

Supplementary materials

Supplementary material associated with this article can be found, in the online version, at doi:10.1016/j.neuroimage.2021.118376.

References

Acosta-Cabronero, J., Betts, M.J., Cardenas-Blanco, A., Yang, S., Nestor, P.J., 2016. In vivo MRI mapping of brain iron deposition across the adult lifespan. J. Neurosci. 36, 364–374.

Acosta-Cabronero, J., Williams, G.B., Cardenas-Blanco, A., Arnold, R.J., Lupson, V., Nestor, P.J., 2013. In vivo quantitative susceptibility mapping (QSM) in Alzheimer's disease. PLoS One 8, e81093.

Barbosa, J.H.O., Santos, A.C., Tumas, V., Liu, M., Zheng, W., Haacke, E.M., Salmon, C.E.G., 2015. Quantifying brain iron deposition in patients with Parkinson's disease using quantitative susceptibility mapping, R2 and R2. Magn. Reson. Imaging 33, 559–565.

Betts, M.J., Acosta-Cabronero, J., Cardenas-Blanco, A., Nestor, P.J., Düzel, E., 2016. High-resolution characterisation of the aging brain using simultaneous quantitative susceptibility mapping (QSM) and R2* measurements at 7 T. Neuroimage 138, 43–63.

Bian, W., Tranvinh, E., Tourdias, T., Han, M., Liu, T., Wang, Y., Rutt, B., Zeineh, M.M., 2016. In Vivo 7T MR quantitative susceptibility mapping reveals opposite susceptibility contrast between cortical and white matter lesions in multiple sclerosis. AJNR Am. J. Neuroradiol. 37, 1808–1815.

Bilgic, B., Pfefferbaum, A., Rohlfing, T., Sullivan, E.V., Adalsteinsson, E., 2012. MRI estimates of brain iron concentration in normal aging using quantitative susceptibility mapping. Neuroimage 59, 2625–2635.

Bilgic, B., Xie, L., Dibb, R., Langkammer, C., Mutluay, A., Ye, H., Polimeni, J.R., Augustinack, J., Liu, C., Wald, L.L., 2016. Rapid multi-orientation quantitative susceptibility mapping. Neuroimage 125, 1131–1141.

Bollmann, S., Rasmussen, K.G.B., Kristensen, M., Blendal, R.G., Østergaard, L.R., Plocharski, M., O'Brien, K., Langkammer, C., Janke, A., Barth, M., 2019. DeepQSM - using deep learning to solve the dipole inversion for quantitative susceptibility mapping. Neuroimage.

Bulk, M., Kenkhuis, B., van der Graaf, L.M., Goeman, J.J., Natté, R., van der Weerd, L., 2018. Postmortem T 2*-weighted MRI imaging of cortical iron reflects severity of alzheimer's disease. J. Alzheimers Dis. 65, 1125–1137.

Chen, L., Soldan, A., Oishi, K., Faria, A., Zhu, Y., Albert, M., van Zijl, P.C.M., Li, X., 2020a. Quantitative susceptibility mapping of brain iron and β-amyloid in MRI and PET relating to cognitive performance in cognitively normal older adults. Radiology, 201603.

Chen, W., Zhu, W., Kovanlikaya, I., Kovanlikaya, A., Liu, T., Wang, S., Salustri, C., Wang, Y., 2014. Intracranial calcifications and hemorrhages: characterization with quantitative susceptibility mapping. Radiology 270, 496–505.

Chen, Y., Jakary, A., Avadiappan, S., Hess, C.P., Lupo, J.M., 2020b. Qsmgan: improved quantitative susceptibility mapping using 3d generative adversarial networks with increased receptive field. Neuroimage 207, 116389.

Damulina, A., Pirpamer, L., Soellradl, M., Sackl, M., Tinauer, C., Hofer, E., Enzinger, C., Gesierich, B., Duering, M., Ropele, S., 2020. Cross-sectional and Longitudinal Assessment of Brain Iron Level in Alzheimer Disease Using 3-T MRI. Radiology 296, 619–626.

De Rochefort, L., Brown, R., Prince, M.R., Wang, Y., 2008. Quantitative MR susceptibility mapping using piece-wise constant regularized inversion of the magnetic field. Magnetic Res. Med. 60, 1003–1009.

Du, L., Zhao, Z., Cui, A., Zhu, Y., Zhang, L., Liu, J., Shi, S., Fu, C., Han, X., Gao, W., 2018. Increased iron deposition on brain quantitative susceptibility mapping correlates with decreased cognitive function in Alzheimer's disease. ACS Chem. Neurosci. 9, 1849–1857.

Gao, Y., Zhu, X., Moffat, B.A., Glarin, R., Wilman, A.H., Pike, G.B., Crozier, S., Liu, F., Sun, H., 2020. xQSM: quantitative susceptibility mapping with octave convolutional and noise-regularized neural networks. NMR Biomed. e4461.

Goodfellow, I., Pouget-Abadie, J., Mirza, M., Xu, B., Warde-Farley, D., Ozair, S., Courville, A., Bengio, Y., 2014. Generative adversarial nets. Adv. Neural Inf. Process. Syst. 27, 2672–2680.

Haacke, E.M., Liu, S., Buch, S., Zheng, W., Wu, D., Ye, Y., 2015. Quantitative susceptibility mapping: current status and future directions. Magn. Reson. Imaging 33, 1–25.

Hammernik, K., Klatzer, T., Kobler, E., Recht, M.P., Sodickson, D.K., Pock, T., Knoll, F., 2017. Learning a variational network for reconstruction of accelerated MRI data. Magn. Reson. Med. 79.

He, K., Zhang, X., Ren, S., Sun, J., 2016. Deep residual learning for image recognition. In: Proceedings of the IEEE Conference on Computer Vision and Pattern Recognition, pp. 770–778.

Jenkinson, M., Smith, S., 2001. A global optimisation method for robust affine registration of brain images. Medical Image Analysis 5, 143–156.

Jung, W., Yoon, J., Ji, S., Choi, J.Y., Kim, J.M., Nam, Y., Kim, E.Y., Lee, J., 2020. Exploring linearity of deep neural network trained QSM: QSMnet+. Neuroimage 211, 116619.

Kames, C., Doucette, J., Rauscher, A., 2019. Proximal variational networks: generalizable deep networks for solving the dipole-inversion problem. 5th International QSM Workshop.

Kelman, C., Ramakrishnan, V., Davies, A., Holloway, K., 2010. Analysis of stereotactic accuracy of the cosman-robert-wells frame and nexframe frameless systems in deep brain stimulation surgery. Stereotact. Funct. Neurosurg. 88, 288–295.

Kingma, D., Ba, J., 2015. Adam: a method for stochastic optimization in. In: Proceedings of the 3rd International Conference for Learning Representations (ICLR'15). San Diego.

Kirilina, E., Helbling, S., Morawski, M., Pine, K., Reimann, K., Jankuhn, S., Dinse, J., Deistung, A., Reichenbach, J.R., Trampel, R., Geyer, S., Müller, L., Jakubowski, N., Arendt, T., Bazin, P.-L., Weiskopf, N., 2020. Superficial white matter imaging: contrast mechanisms and whole-brain in vivo mapping. Sci. Adv. 6, eaaz9281.

Kressler, B., De Rochefort, L., Liu, T., Spincemaille, P., Jiang, Q., Wang, Y., 2009. Nonlinear regularization for per voxel estimation of magnetic susceptibility distributions from MRI field maps. IEEE Trans. Med. Imaging 29, 273–281.

Kuchel, P., Chapman, B., Bubb, W., Hansen, P.E., Durrant, C., Hertzberg, M., 2003. Magnetic susceptibility: solutions, emulsions, and cells. Concepts Magnet. Res. Part A 18, 56–71.

Lai, K.W., Aggarwal, M., van Zijl, P., Li, X., Sulam, J., 2020. Learned proximal networks for quantitative susceptibility mapping. Med Image Comput. Comput. Assist. Interv. 12262, 125–135.

Landis, J.R., Koch, G.G., 1977. The measurement of observer agreement for categorical data. Biometrics 33, 159–174.

Langkammer, C., Schweser, F., Shmueli, K., Kames, C., Li, X., Guo, L., Milovic, C., Kim, J., Wei, H., Bredies, K., 2018. Quantitative susceptibility mapping: report from the 2016 reconstruction challenge. Magn. Reson. Med. 79, 1661–1673.

Li, X., Harrison, D.M., Liu, H., Jones, C.K., Oh, J., Calabresi, P.A., van Zijl, P.C., 2016. Magnetic susceptibility contrast variations in multiple sclerosis lesions. J. Magn. Reson. Imaging 43, 463–473.

Li, X., Vikram, D.S., Lim, I.A.L., Jones, C.K., Farrell, J.A.D., Zijl, P.C.M.V., 2012. Mapping magnetic susceptibility anisotropies of white matter in vivo in the human brain at 7T. Neuroimage 62.

Liu, C., 2010. Susceptibility tensor imaging. Magn. Reson. Med. 63, 1471–1477.

Liu, C., Li, W., Tong, K.A., Yeom, K.W., Kuzminski, S., 2015. Susceptibility-weighted imaging and quantitative susceptibility mapping in the brain. J. Magn. Reson. Imaging 42, 23–41.

Liu, J., Liu, T., de Rochefort, L., Ledoux, J., Khalidov, I., Chen, W., Tsiouris, A.J., Wisnieff, C., Spincemaille, P., Prince, M.R., 2012. Morphology enabled dipole inversion for quantitative susceptibility mapping using structural consistency between the magnitude image and the susceptibility map. Neuroimage 59, 2560–2568.

Liu, T., Spincemaille, P., De Rochefort, L., Kressler, B., Wang, Y., 2009. Calculation of susceptibility through multiple orientation sampling (COSMOS): a method for conditioning the inverse problem from measured magnetic field map to susceptibility source image in MRI. Magnetic Resonance Med. 61, 196–204.

Lotfipour, A.K., Wharton, S., Schwarz, S.T., Gontu, V., Schäfer, A., Peters, A.M., Bowtell, R.W., Auer, D.P., Gowland, P.A., Bajaj, N.P., 2012. High resolution magnetic susceptibility mapping of the substantia nigra in Parkinson's disease. J. Magn. Reson. Imaging 35, 48–55.

Parikh, N., Boyd, S., 2014. Proximal algorithms. Found. Trends Optimiz. 1, 127–239.

Polak, D., Chatnuntawech, I., Yoon, J., Iyer, S.S., Bilgic, B., 2019. Nonlinear Dipole Inversion (NDI) enables Quantitative Susceptibility Mapping (QSM) without parameter tuning.

Rasouli, J., Ramdhani, R., Panov, F.E., Dimov, A., Zhang, Y., Cho, C., Wang, Y., Kopell, B.H., 2018. Utilization of quantitative susceptibility mapping for direct targeting of the subthalamic nucleus during deep brain stimulation surgery. Operative Neurosurg. 14, 412–419.

Ravishankar, S., Bresler, Y., 2011. MR image reconstruction from highly undersampled k-space data by dictionary learning. IEEE Trans. Med. Imaging 30, 1028.

Ronneberger, O., Fischer, P., Brox, T., 2015. U-net: Convolutional networks for biomedical image segmentation. In: International Conference on Medical image computing and computer-assisted intervention. Springer, pp. 234–241.

Schofield, M.A., Zhu, Y., 2003. Fast phase unwrapping algorithm for interferometric applications. Opt. Lett. 28, 1194–1196.

Schweser, F., Deistung, A., Sommer, K., Reichenbach, J.R., 2013. Toward online reconstruction of quantitative susceptibility maps: superfast dipole inversion. Magn. Reson. Med. 69, 1581–1593.

Shmueli, K., de Zwart, J.A., van Gelderen, P., Li, T.Q., Dodd, S.J., Duyn, J.H., 2009. Magnetic Susceptibility Mapping of Brain Tissue In Vivo Using MRI Phase Data. Magn. Reson. Med. 62, 1510–1522.

Shmueli, K., Dodd, S.J., Li, T.Q., Duyn, J.H., 2011. The contribution of chemical exchange to MRI frequency shifts in brain tissue. Magn. Reson. Med. 65, 35–43.

Smith, S.M., 2002. Fast robust automated brain extraction. Hum. Brain Mapp. 17, 143–155.

Szegedy, C., Vanhoucke, V., Ioffe, S., Shlens, J., Wojna, Z., 2016. Rethinking the inception architecture for computer vision. In: Proceedings of the IEEE Conference on Computer Vision and Pattern Recognition, pp. 2818–2826.

van Duijn, S., Bulk, M., van Duinen, S.G., Nabuurs, R.J., van Buchem, M.A., van der Weerd, L., Natté, R., 2017. Cortical iron reflects severity of Alzheimer's disease. J. Alzheimers Dis. 60, 1533–1545.

Wang, Y., Liu, T., 2015. Quantitative susceptibility mapping (QSM): decoding MRI data for a tissue magnetic biomarker. Magn. Reson. Med. 73, 82–101.

Wei, H., Cao, S., Zhang, Y., Guan, X., Yan, F., Yeom, K.W., Liu, C., 2019a. Learning-based single-step quantitative susceptibility mapping reconstruction without brain extraction. Neuroimage 202, 116064.

Wei, H., Dibb, R., Zhou, Y., Sun, Y., Xu, J., Wang, N., Liu, C., 2015. Streaking artifact reduction for quantitative susceptibility mapping of sources with large dynamic range. NMR Biomed. 28, 1294–1303.

Wei, H., Zhang, C., Wang, T., He, N., Li, D., Zhang, Y., Liu, C., Yan, F., Sun, B., 2019b. Precise targeting of the globus pallidus internus with quantitative susceptibility mapping for deep brain stimulation surgery. J. Neurosurg. 1, 1–7.

Wharton, S., Bowtell, R., 2010. Whole-brain susceptibility mapping at high field: a comparison of multiple-and single-orientation methods. Neuroimage 53, 515–525.

Wharton, S., Bowtell, R., 2012. Fiber orientation-dependent white matter contrast in gradient echo MRI. Proc. Natl. Acad. Sci. 109, 18559–18564.
Wu, B., Li, W., Guidon, A., Liu, C., 2012. Whole brain susceptibility mapping using compressed sensing. Magn. Reson. Med. 67, 137–147.
Yoon, J., Gong, E.H., Chatnuntawech, I., Bilgic, B., Lee, J., Jung, W., Ko, J., Jung, H., Setsompop, K., Zaharchuk, G., Kim, E.Y., Pauly, J., Lee, J., 2018. Quantitative susceptibility mapping using deep neural network: QSMnet. Neuroimage 179, 199–206.
Zhang, Y., Shi, J., Wei, H., Han, V., Zhu, W.-Z., Liu, C., 2019. Neonate and infant brain development from birth to 2 years assessed using MRI-based quantitative susceptibility mapping. Neuroimage 185, 349–360.
Zhang, Y., Wei, H., Cronin, M.J., He, N., Yan, F., Liu, C., 2018. Longitudinal atlas for normative human brain development and aging over the lifespan using quantitative susceptibility mapping. Neuroimage 171, 176–189.
Zhou, W., Bovik, A.C., Sheikh, H.R., Simoncelli, E.P., 2004. Image quality assessment: from error visibility to structural similarity. IEEE Trans. Image Process. 13, 600–612.
Zuo, X.N., Xing, X.X., 2014. Test-retest reliabilities of resting-state FMRI measurements in human brain functional connectomics: a systems neuroscience perspective. Neurosci. Biobehav. Rev. 45, 100–118.